Title

Design and Mechanics of Cable-Driven Rolling Diaphragm Transmission

Author

Lam, Hoi Man

Publication Date

2023

UNIVERSITY OF CALIFORNIA SAN DIEGO

Design and Mechanics of Cable-Driven Rolling Diaphragm Transmission

A thesis submitted in partial satisfaction of the
requirements for the degree
Masters of Science

in

Mechanical Engineering

by

Hoi Man Lam

Committee in charge:

Professor Michael C. Yip, Chair
Professor Raymond A. de Callafon
Professor Tania Morimoto

2023

The thesis of Hoi Man Lam is approved, and it is acceptable in quality and form for publication on microfilm and electronically.

University of California San Diego

2023

TABLE OF CONTENTS

LIST OF FIGURES

LIST OF TABLES

ACKNOWLEDGEMENTS

Thanks to Dr Yip, Dimitri, and Florian, whose experience and passion for robotics I've tried to emulate.

Thanks to my friends during my time at UCSD, and to the experiences, stresses, and laughs we shared.

Thanks to my parents, who supported me and gave me the freedom to pursue whatever I chose.

Chapters 1, 2, 3, and 4, in part, has been submitted for publication of the material as it may appear in ICRA 2023, Hoi Man Lam, W. Jared Walker, Lucas Jonasch, Dimitri Schreiber, and Michael C. Yip, IEEE 2023. The thesis author was the primary investigator and author of this paper.

VITA

2021	B. S. in Mechanical Engineering, University of California San Diego
2022	M. S. in Mechanical Engineering, University of California San Diego

PUBLICATIONS

"ARCSnake: An Archimedes' Screw-Propelled, Reconfigurable Serpentine Robot for Complex Environments", 2020 IEEE International Conference on Robotics and Automation (ICRA), 2020, pp. 7029-7034, doi: 10.1109/ICRA40945.2020.9196968.

"ARCSnake: Reconfigurable Snakelike Robot With Archimedean Screw Propulsion for Multidomain Mobility", in IEEE Transactions on Robotics, vol. 38, no. 2, pp. 797-809, April 2022, doi: 10.1109/TRO.2021.3104968.

ABSTRACT OF THE THESIS

Design and Mechanics of Cable-Driven Rolling Diaphragm Transmission

by

Hoi Man Lam

Masters of Science in Mechanical Engineering

University of California San Diego, 2023

Professor Michael C. Yip, Chair

Applications of rolling diaphragm transmissions for medical and teleoperated robotics are of great interest, due to the low friction of rolling diaphragms combined with the power density and stiffness of hydraulic transmissions. However, the stiffness-enabling pressure preloads can form a tradeoff against bearing loading in some rolling diaphragm layouts, and transmission setup can be difficult. Utilization of cable drives compliment the rolling diaphragm transmission's advantages, but maintaining cable tension is crucial for optimal and consistent performance.

In this thesis, a coaxial opposed rolling diaphragm layout with cable drive and an electronic transmission control system are investigated, with a focus on system reliability and scalability. Mechanical features are proposed which enable force balancing, decoupling of transmission pressure from bearing loads, and maintenance of cable tension. Key considerations and procedures for automation of transmission setup, phasing, and operation are also presented. An analysis of system stiffness is presented to identify key compliance contributors, and experiments are conducted to validate prototype design performance.

1 Introduction

In this thesis, the design, prototyping, modelling, and characterization of a coaxial enclosed cable-driven rolling diaphragm transmission is detailed. Before exploring the key novel features of the design, a baseline understanding of rolling diaphragms and how they are used in hydraulic transmissions is needed to motivate the design choices for the proposed actuator.

1.1 Rolling Diaphragm Transmissions

1.1.1 Composition of a Rolling Diaphragm

A rolling diaphragm is a flexible seal usually composed of fiber-reinforced rubber, and acts as a deformable wall for a pressure vessel. The diaphragm is enclosed by cylindrical walls, and wraps around a piston. The axial pressure forces are mostly applied to the rolling diaphragm surface against the piston face, while a smaller portion fills out the rolling diaphragm convolution (Fig. 1.1a).

If the reaction force of the piston is lower than the applied axial pressure force on the piston face, the piston translates axially along the cylinder centerline, while the outer and inner diaphragm walls roll along the cylindrical enclosure and piston sides respectively (Fig. 1.1c). This motion only introduces rolling friction and no sliding friction, lowering the overall inherent friction involved in actuating the piston when compared to O-ring sealed pistons.

The cylindrical walls and piston also ensure that as pressure is introduced, the pressure is evenly distributed radially, either pushing outwards on the outer diaphragm

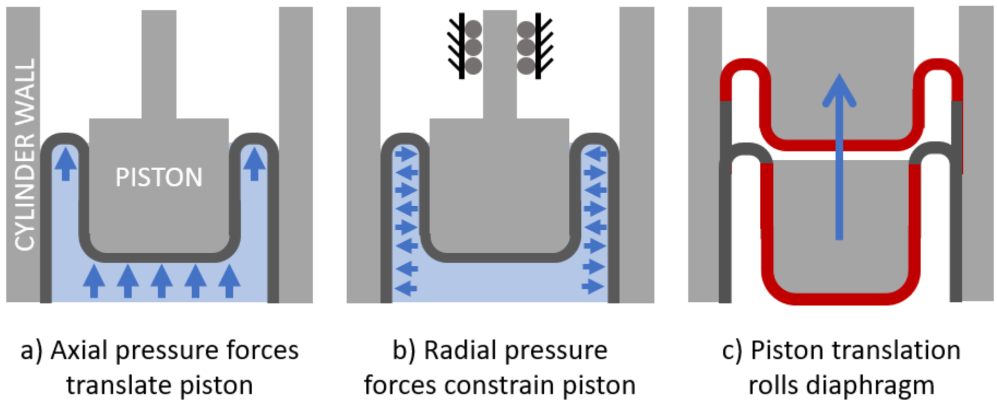

Figure 1.1: Diagram of rolling diaphragm operation. Axial pressure forces translate the piston (a), while radial pressure forces form a self-centering effect on the piston (b). The rolling diaphragm's convolution rolls along the piston and cylinder walls during translation, such that there is only rolling friction and no sliding friction (c).

fold which is braced by the cylindrical wall, or inwards on the inner diaphragm fold braced by the piston . This evenly distributed radial pressure force causes a self-centering effect on the piston, as any moment on the piston causes induces a restoring force from the fluid pressure (Fig. 1.1b). The self-centering effect allows for the diaphragm to provide some degree of linear bearing functionality, though the effect decreases as the amount of diaphragm contacting the piston wall decreases towards the extremity of the range of motion.

Lastly, the fully sealed nature of the rolling diaphragm prevents pressure blow-by effects, ensuring no transmission fluid leakage. However, the diaphragms are somewhat permeable depending on the material, which can lead to slight transmission fluid loss over long periods of time.

1.1.2 Transmissions using Rolling Diaphragms

When rolling diaphragms are used to cap either end of a constant volume of transmission fluid, a rolling diaphragm transmission is formed. With one rolling diaphragm transmission, assuming both ends are identical, a positive translation of the diaphragm on one end causes an equal positive translation on the other end. However, the transmission must operate with positive pressure, in order to avoid pulling the diaphragm away from the enclosure or piston walls and causing a jam. This means that one can only 'push' the transmission from either end if there is only one rolling diaphragm transmission line. One way to allow bidirectional control is to introduce a preload force on either end of the transmission, which maintains a baseline positive pressure on the transmission fluid, such as by mounting springs against the pistons. However, springs impart a varying force depending on it's displacement, leading to a varying preload force over the transmission's range of motion.

Another method is to use a two rolling diaphragm transmission lines. The first line is filled with pressurized air, and the second line is filled with an incompressible transmission fluid. The pistons of both lines are mechanically coupled such that the pressurized air in the first line acts as the preload force for the incompressible second line. Using a pressurized air rolling diaphragm transmission as the preload allows for constant preload force no matter the piston position, as the preload force is only a function of axial surface area and fluid pressure, both of which are held constant. This pressurized air line can also be shared across multiple diaphragm transmission lines in what is called a "N+1" configuration, so long as the air pressure can be regulated consistently across the increased air line volume [WCMH16].

With a paired rolling diaphragm transmission, the load capacity is equal to the preload pressure, as applying a load that causes a pressure difference which exceeds the positive pressure preload will lead to jamming and failure to roll the diaphragms. Therefore, the maximum load capacity is half of the rated pressure of the rolling diaphragms, if the preload pressure is also set to half of the rated pressure. The rated pressure of rolling diaphragms are usually fairly high, due to the fiber reinforcement of the diaphragms which make them strong under stretch.

1.1.3 Applications of Rolling Diaphragms

Rolling diaphragms have been applied to many applications, such as in medical or teleoperated robotics. In medical applications, rolling diaphragm transmissions have found great use in MR-safe robots, which make surgery during live scans possible by allowing the MR-incompatible actuator to power the robot from outside the MR field [DGL+19], [DGL+17], [GDL+18], [FIS+21]. The usage of rolling diaphragm transmissions also provides smooth force transmission in a compact package, which is important for patient comfort, and accommodation of a variety of patient sizes.

The hydrostatic rolling diaphragm transmission itself was investigated in various works, where some works modelled the transmission as a second-order spring model [DGL+19], [GFC19], [DPG21]. John Peter Whitney proposed a N+1 hybrid hydrostatic transmission setup, utilizing N hydraulic lines and 1 common pneumatic preload line, which minimizes transmission complexity without hampering performance [WCMH16], [WGBH14], [MW19].

Whitney's designs featured a belt-driven design for rotary actuation, and a linkage design for directly actuating a finger, to convert the transmission's translational motion into the desired mechanical work. In the linkage hand design, the load is attached to the diaphragm piston through the air-side diaphragm, introducing a dynamic seal, which can be tolerance-intensive and introduces constant pressure leakage.

In another variation of the rolling diaphragm transmission, an alternative cable-driven floating-cylinder design was investigated for use in wearable robotic limbs [VDL+20], [KCGP20]. The cable drive provides reduced friction and backlash to accentuate the rolling diaphragm transmission's transparency and backdrivability, while the floating-cylinder layout makes use of the self-aligning features of the rolling diaphragm.

1.2 Proposed Design

In this thesis, an alternative coaxial rolling diaphragm transmission design is investigated, which retains proven features such as the N+1 hybrid transmission layout, and a cable drive for its ability to minimize backlash and friction forces. Building on top of those elements, the following are introduced:

1. A translating inner core inline with the rolling diaphragm, coupled with a force-balanced angled cable drive design, which decouples transmission pressure from cable

tension and friction, reduces bearing load thanks to cable preload tension balancing, and provides a constant mechanical advantage over a range of motion beyond a full rotation.

2. A method for individual transmission component stiffness analysis to predict full system stiffness and key compliance contributors.

3. An electronic fluid transmission control system for automated pressure and phasing regulation and control.

1.3 Acknowledgements

Chapter 1, in part, has been submitted for publication of the material as it may appear in ICRA 2023, Hoi Man Lam, W. Jared Walker, Lucas Jonasch, Dimitri Schreiber, and Michael C. Yip, IEEE 2023. The thesis author was the primary investigator and author of this paper.

2 Mechanical Design

2.1 Overview

The transmission consists of two identical paired units, where each unit uses two rolling diaphragms to interface with the two air or water transmission lines. The identical pairing means there is no reduction or difference in performance between the input and output actuators.

In each transmission unit (Fig. 2.1a), a cable drive converts the fluid-driven linear rolling diaphragm motion to rotary input-output motions for robotic joints. A linearly translating core actuates that cable drive, while isolating the transmission pressure forces from the cable tension and central pillar bearings. Lastly, a stationary frame provides structural support and alignment between rolling diaphragms and translating core.

2.2 Actuator Design

2.2.1 Cable Drive and Translating Core

A cable drive was chosen due to its inherent advantages of low friction, low backlash, and high stiffness [BI10]. In the prototype transmission, a 1/16" diameter 302 stainless steel cable with 7x19 construction was chosen for its high flexibility, and sufficient breaking strength of $2100N$ to match the maximum supportable load of $600N$. The maximum supportable force is a function of maximum rated diaphragm pressure $P_{max} = 1.7MPa$, and diaphragm piston radius $r_{piston} = 15mm$ in Eqn. 2.1. The corresponding maximum

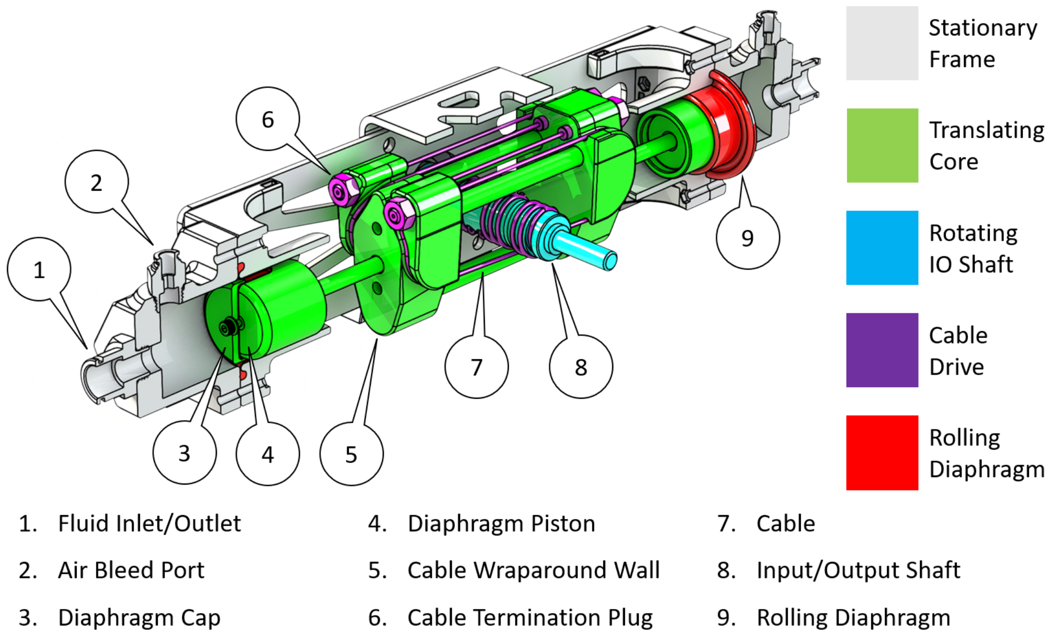

(a) Section view of one actuator unit.

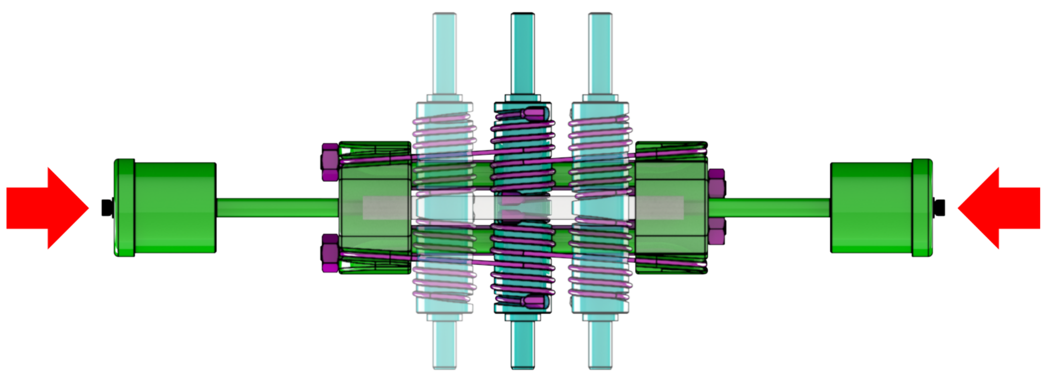

(b) Translating capstan pillar relative to the core.

Figure 2.1: Mechanical design of one actuator unit. (a) shows the section view. Fluid pressure difference between the two rolling diaphragms (red) actuate the translating core (green), which drives the input/output shaft (cyan) through the cable drive (purple). The coaxial rolling diaphragms are fully sealed, and the translating core maintains cable tension even when the system is depressurized. (b) shows how the capstan pillar rolls relative to the core; once the pillar is fixed to the housing via bearings, the core linearly translates. Cable drive fleet angle is kept constant across the full range of motion through the geometry of the capstan pillar and the cable wrap-around walls, maintaining constant cable tension for controllability. Fluid line pressure preload forces are coaxially balanced through the translating core.

supportable torque is $6Nm$ for a capstan radius of $r_{capstan} = 10mm$.

$$F_{max} = \frac{P_{max}}{2}(\pi r_{piston}^2) \tag{2.1}$$

Due to the limited travel of the rolling diaphragm, there is a direct tradeoff between the diameter of a flat cable pulley and the angular range of motion. However, wrapping the cable helically up a capstan pillar allows for increased capstan effect and more than one rotation of motion despite limited diaphragm travel.

Within the cable drive, the cables are run at an angle enforced by wall and capstan geometry throughout the full range of motion (Fig. 2.1b). The fleet angle is kept constant by terminating the cables with the same angle as the helix pitch. Constant fleet angle is necessary to maintain constant cable tension for a linear performance, which is useful in direct teleoperation applications.

The cable drive's forces are balanced by the symmetrical placement of cable angle and departure locations, which decouples cable preload tension from bearing loading. The free body diagram moment balance of Fig. 2.2 sums to 0, indicating full cancellation:

$$\Sigma M_y = T_L r_L - T_L r_L + T_R r_R - T_R r_R = 0 \tag{2.2}$$

Where T_L and r_L are the cable preload tension force and moment arm on the left side of the capstan, and T_R and r_R on the right side. High cable preload tension is preferred to improve axial stiffness, which decreases with load range to preload ratio [HR96].

The translating core structure fixes the cable terminations and absorbs the transmission pressure between the two rolling diaphragms. One drawback to cable drives can be the difficulty in tuning and maintaining cable tension, which is a prerequisite for consistent performance. By fixing the cable terminations within the rigid core structure, the cables can be preloaded at high tension, allowing for low slack and high stiffness [BI10]. Cable tension is held even when the transmission is depressurized, which is advantageous in medical settings, where surgeons might not have the expertise or tools to troubleshoot and repair cable slack issues. The prototype translating core comprises of solid 3D printed termination walls in Markforged Onyx filament and carbon fiber rods.

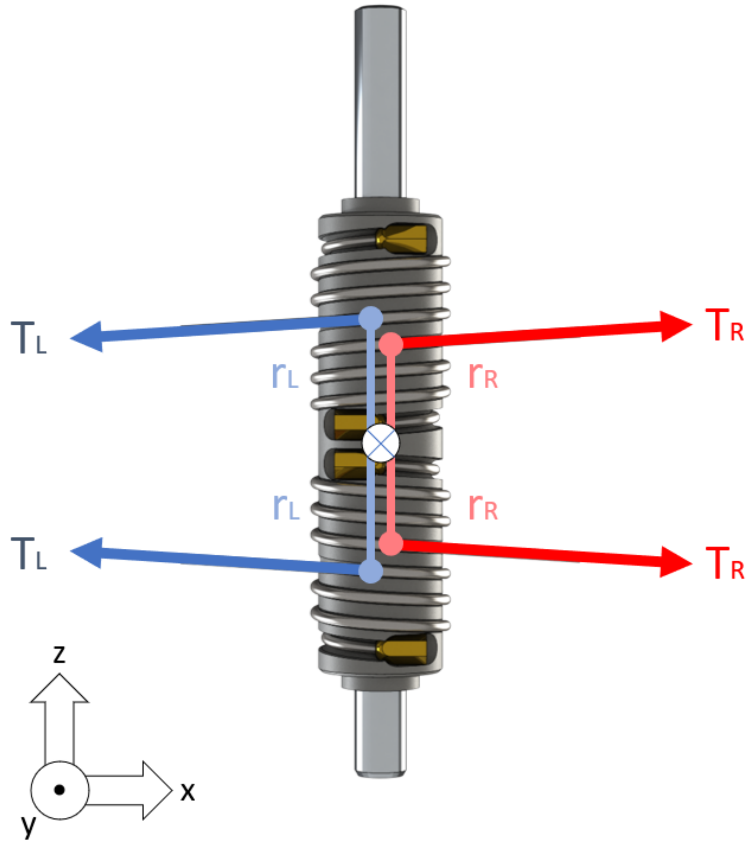

Figure 2.2: Cable tension forces are symmetrically balanced, thereby eliminating moment bearing loads in the y-axis (out of page) and decoupling cable tension from axial bearing loads in x/y directions.

2.2.2 Coaxial Enclosed Rolling Diaphragm Layout

Interacting with the fluid transmission lines, rolling diaphragms interface with coaxial pistons on either side of the translating core. Rolling diaphragms are flexible seals that extend and retract via a rolling action, eliminating the sliding friction that typical piston O-Ring seals have [mar]. The rolling diaphragms used in the prototype are DM3-35-35 rolling diaphragms manufactured by IER Fujikura, with stroke of 46mm, diameter of 35mm, and maximum pressure rating of $1.7MPa$.

Both fluid transmission lines have a pressure preload, which fills out the rolling diaphragm's convolution to prevent jamming, enables high fluid stiffness, and determines transmission load capacity. This transmission preload pressure has a much higher magnitude of force relative to the magnitude of input/output force transferred.

In the proposed transmission, the two rolling diaphragms are aligned in a coaxial opposed layout, such that preload pressures are balanced against one another (Fig. 2.1b). These preload pressure forces compress the translating core, but are isolated from bearings by the cable drive, decoupling transmission pressure from bearing friction. The cable drive is situated between the diaphragm pistons, keeping both fluid chambers fully enclosed to avoid pressure leakage.

2.3 Transmission Design

2.3.1 Hydrostatic Transmission

Two identical actuators connected by a hydraulic line form one transmission system, detailed in Fig. 2.3. The hydraulic line acts as an incompressible link between the actuator, while an opposing pneumatic line provides a preload pressure on the water line. The water can be thought of as a solid rod linking the actuators, and the amount of water as the length of the rod. The phase offset may be adjusted, and therefore eliminated, by adding or removing water from the line. High preload pressures help dissolve remaining air into the water to achieve a stiff and responsive system.

The volume of water in the hydraulic line determines the phase offset between the input and output shafts. Manual alignment is time consuming and difficult, and misaligned actuators may hit their endstops prematurely resulting in reduced range of motion and control. Automation of this phasing process removes a large hurdle for system adoption, and effectively negates long-term issues such as minuscule leaks and settling. It also reduces misalignment factors like tube and cable flex by allowing phasing at a high pressure, close to the standard operating preload pressure.

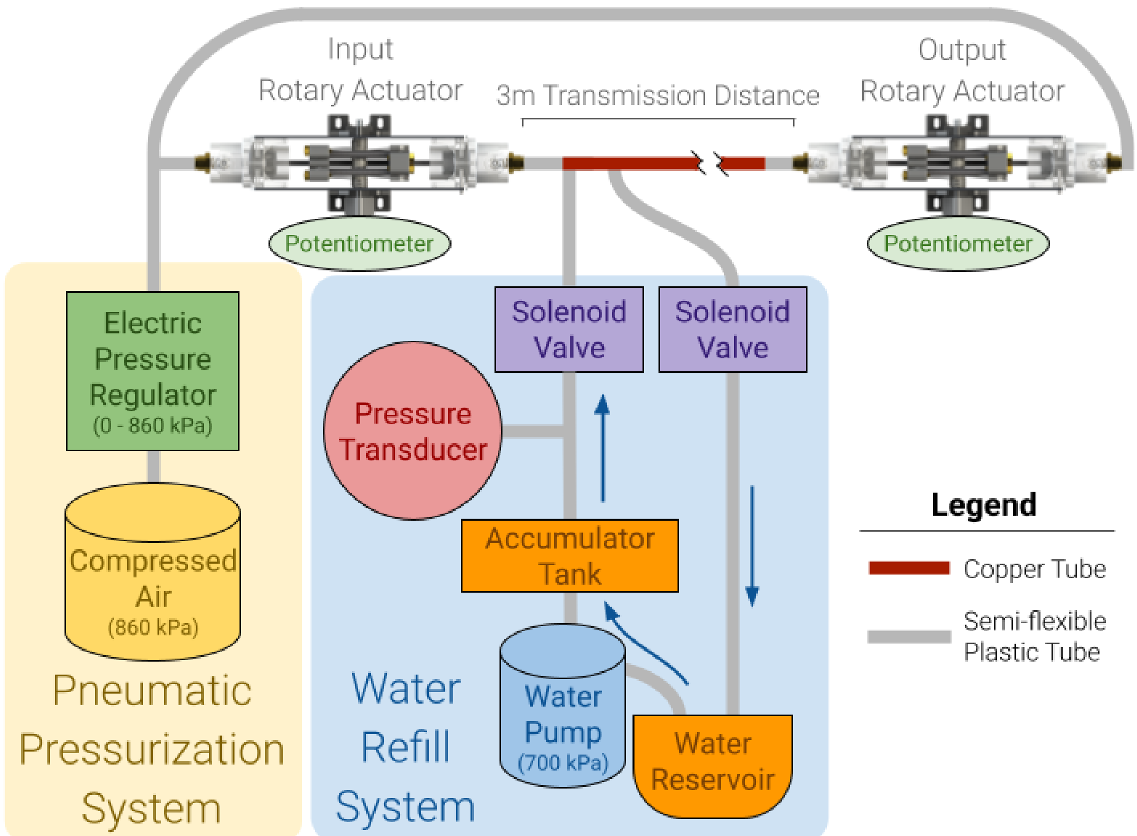

Figure 2.3: Transmission system setup. Stiffness is maximized along the hydraulic transmission distance by using a copper tube, while small sections of flexible plastic tube at each end allow for some flexibility in actuator placement. The incoming water line is maintained at $700kPa$ by a water pump. The outgoing line releases into a depressurized reservoir which feeds into the pump. The preload pressure is controlled through a proportional electric pressure regulator, which allows for precise pressure control anywhere from 0 to $860kPa$. The design is intended for an N+1 configuration (introduced in [WCMH16]), such that multiple transmissions are preloaded by one single pneumatic line, simplifying scalability.

2.3.2 Predictive Phasing

The microcontroller phases the actuators efficiently through a proportional controller, calculating the adjustment that is needed to rotationally align the actuators. The flow rate Q through a solenoid valve is given by:

$$Q = K_v \sqrt{\Delta P} \tag{2.3}$$

where ΔP is the pressure drop and K_v the flow factor of the valve. The relationship between water volume and phase offset was determined empirically, resulting in the following relationship:

$$V_W = \frac{|\Delta \phi|}{9.594} \tag{2.4}$$

where V_W is water volume in mL and $\Delta \phi$ is the phase offset in degrees. By combining Eq. 2.3 and 2.4, the time the solenoid valve should be opened is found. The sign of the phase offset $\Delta \phi$ determines if the intake or outlet valve should be used.

$$t = \frac{V_W}{Q} = \frac{|\Delta \phi|}{9.594 K_v \sqrt{\Delta P}} \tag{2.5}$$

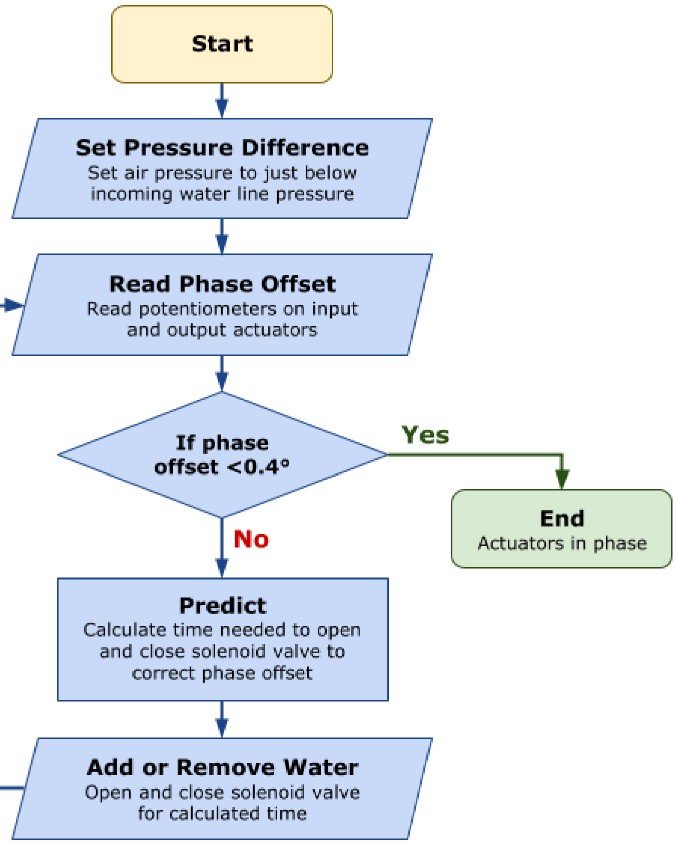

Figure 2.4: Automatic phasing algorithm. ΔP of $15kPa$, along with potentiometer accuracy and solenoid valve response time, resulted in a $0.4°$ acceptable maximum phase offset for our setup.

Fig. 2.4 shows the actuator phasing algorithm. The alignment resolution is limited by the ΔP from the water refill system to the transmission line. To achieve finer angle adjustments, the transmission pressure is brought to just below the water injection pressure to decrease ΔP. This increases ΔP for water ejection, but it is inconsequential since any overshoot can be corrected by water injection.

2.3.3 Automated Operation

The system operating procedure is outlined in Fig. 2.5. Users operate the system through a text-based interface with a microcontroller. Plain language instructions and commands allow even a non-technical user to set up and adjust a transmission. An air bleed mode removes air bubbles that entered the water line during assembly. When not in operation, the system is stored in a hibernation state rather than completely removing all water and air pressure. Maintaining the system at a low pressure (for example, $100kPa$) removes the need to bleed air from the water lines or reseat the rolling diaphragms. Completely depressurizing the actuator is used to disassemble or move the transmission setup.

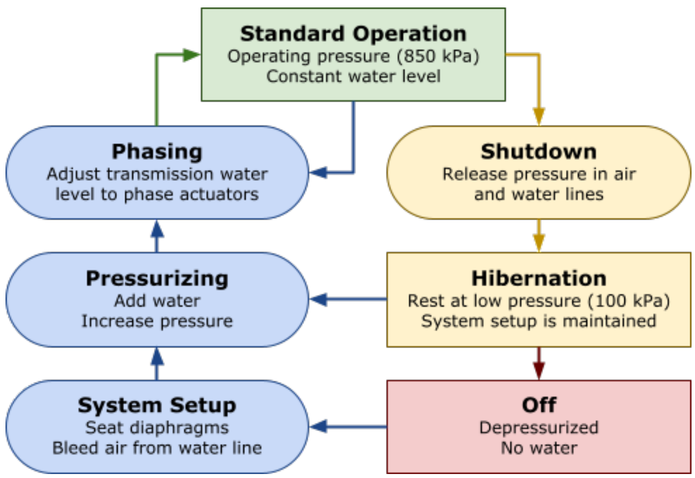

Figure 2.5: Operating procedure for the transmission system. Ovals represent transitory steps that lead to steps intended to be used for extended periods of time, represented by rectangles.

2.4 Acknowledgements

Chapter 2, in full, has been submitted for publication of the material as it may appear in ICRA 2023, Hoi Man Lam, W. Jared Walker, Lucas Jonasch, Dimitri Schreiber, and Michael C. Yip, IEEE 2023. The thesis author was the primary investigator and author of this paper.

3 Transmission Analysis

3.1 Component Compliance Analysis

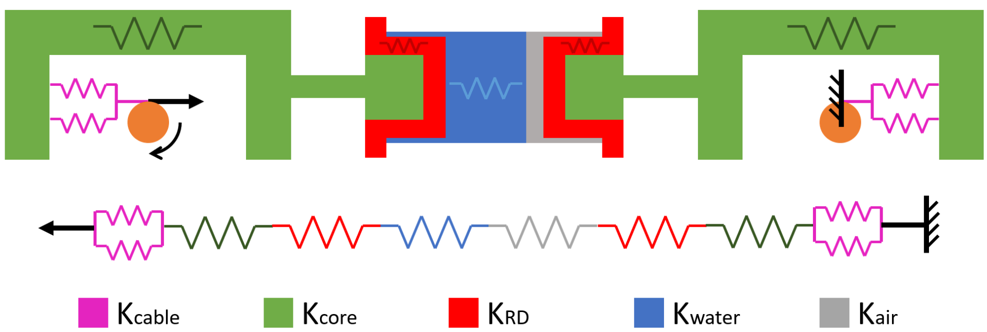

Figure 3.1: Transmission stiffness system model, assuming locked output shaft and torqued input shaft applying a force into the system. The model assumes some proportion of undissolved air left in the system, which acts as an additional spring in series in the fluid transmission.

To predict the transmission stiffness and identify the main compliance contributors in the system, a simple spring system, as illustrated in Fig. 3.1, was used to model the transmission. Fluid stiffness and cable stiffness are determined analytically, while more complex components such as the translating core and diaphragm stiffnesses are determined respectively using FEA and empirical methods. The system assumes that the change in force is applied by the input side capstan pillar, while the output side capstan pillar is locked.

Table 3.1: Theoretical fluid line stiffness variables

Variable	**Value**	**Description**
E_{water}	2.20 $[GPa]$	Bulk modulus of water
E_{air}	1.42 $[GPa]$	Bulk modulus of air
A_{cyl}	9.62E-4 $[m^2]$	Cross section of diaphragm cylinder
A_{hose}	3.17E-5 $[m^2]$	Cross section of hose
L_{cyl}	3.80E-2 $[m]$	Length of diaphragm cylinder
L_{hose}	4.26E-2 $[m]$	Length of hose
p_{water}	0.99 [%]	Proportion of water in transmission
p_{air}	0.01 [%]	Proportion of air in transmission
K_{water}	1.58E6 $[N/m]$	Est. K of fluid line water
K_{air}	3.99E3 $[N/m]$	Est. K of fluid line undissolved air

The fluid transmission stiffness is separated into a water stiffness (K_{air}) and air stiffness (K_{air}), assuming there is some proportion of undissolved air p_{air} in the system. These fluid stiffnesses were found using Eq. 3.1 and the variables in Table 3.1.

$$K_{fluid} = [p(2\frac{L_{cyl}}{A_{cyl}E_{fluid}} + \frac{L_{hose}}{A_{hose}E_{fluid}})]^{-1} \tag{3.1}$$

Cable stiffness (K_{cable}) was calculated with Eq. 3.2 Where A_{cable} is the cable's cross-section, L_{cable} is the cable length between the capstan and the wrap-around wall, and E_{cable} is $200GPa$ for 304 stainless steel.

$$K_{cable} = \frac{E_{cable}A_{cable}}{L_{cable}} \tag{3.2}$$

For both rolling diaphragm stiffness (K_{RD}) and translating core stiffness (K_{core}), the stiffness was estimated via $K = \frac{\Delta F}{\Delta x}$, where ΔF and Δx are the change in force and deflection respectively. For K_{RD}, the rolling diaphragm stretch under force application was measured on a material test system. And for K_{core}, the deflection of the cable termination point under a unit applied force was estimated via FEA (Fig. 3.2).

The resultant transmission stiffness estimate is a combination of the individual component stiffness estimates:

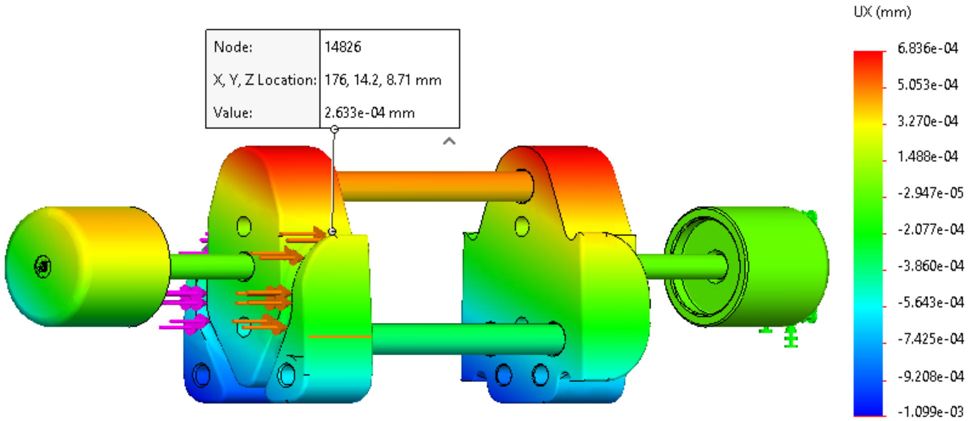

Figure 3.2: FEA estimated cable termination deflection from application of $1N$ from cables.

$$K_{tot} = (\frac{1}{K_{cable}} + \frac{2}{K_{core}} + \frac{2}{K_{RD}} + \frac{1}{K_{water}} + \frac{1}{K_{air}})^{-1} \tag{3.3}$$

Where the individual estimates and overall stiffness estimate are featured in Table 3.2. Of the individual stiffnesses, the rolling diaphragm and undissolved air contribute the most to overall compliance. The equivalent estimated angular stiffness over a $20mm$ diameter capstan pillar is $23.54 Nm/rad$, using $K_{rot} = K_{lin} r^2$. However, the stiffness value can vary greatly with p_{air}, as shown in Fig. 3.3.

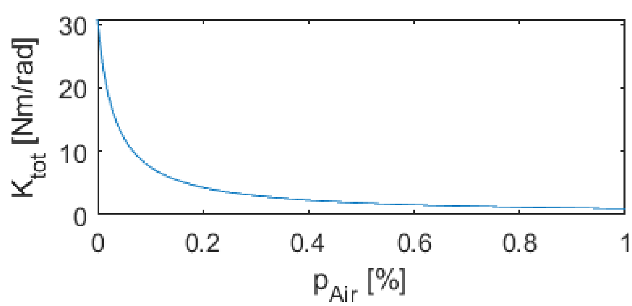

Figure 3.3: Theoretical transmission stiffness as a function of undissolved air % remaining in fluid line.

Table 3.2: Theoretical component stiffness values, and resultant total transmission stiffness assuming p_{air} of 0.01 %.

Source	**Variable**	**Stiffness** $[N/m]$	**% Compliance**
Water in fluid line	K_{water}	1.54E6	15.2%
Undissolved air in fluid line	K_{air}	9.97E5	23.6%
Cable drive	K_{cable}	8.98E6	2.60%
Translating core	K_{core}	3.80E6	12.4%
Rolling diaphragm	K_{RD}	1.02E6	46.1%
Full Transmission	K_{total}	2.35E5	

3.2 System Modelling

3.2.1 State Space Model

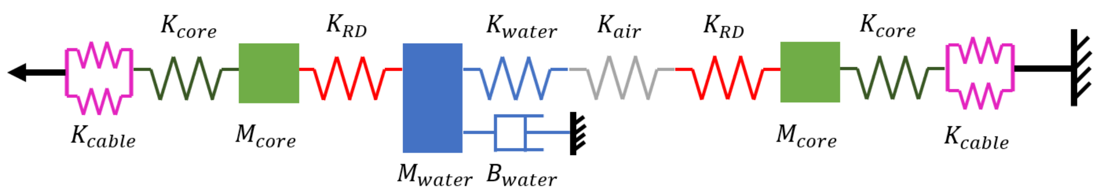

Figure 3.4: Transmission spring system model. Cable, rolling diaphragm, and air mass is considered negligible. Frictional effects from the cable drive and core are also considered negligible.

As shown in Fig 3.4, a system model of the transmission was developed by considering the transmission as a mass-spring system with three main masses, the cores on either actuator, and the water within the transmission line. The other masses in the transmission, such as cable and rolling diaphragm mass, are considered to be negligible. The frictional and damping effects for the cable drive and rolling diaphragm are also considered negligible in this system. A state space system of the form

$$\dot{x} = Ax + Bu, \qquad y = Cx + Du$$

was derived, with the corresponding matrices and vectors shown below:

.

$$\begin{bmatrix} v_1 \\ a_1 \\ v_2 \\ a_2 \\ v_3 \\ a_3 \end{bmatrix} = \begin{bmatrix} 0 & 1 & 0 & 0 & 0 & 0 \\ \frac{-k_{12}}{m_{core}} & 0 & \frac{k_{12}}{m_{core}} & 0 & 0 & 0 \\ 0 & 0 & 0 & 1 & 0 & 0 \\ \frac{k_{12}}{m_{water}} & 0 & -\frac{k_{12}+k_{23}}{m_{water}} & \frac{-b_{water}}{m_{water}} & \frac{k_{23}}{m_{water}} & 0 \\ 0 & 0 & 0 & 0 & 0 & 1 \\ 0 & 0 & \frac{k_{23}}{m_{core}} & 0 & \frac{-k_{23}+k_{34}}{m_{core}} & 0 \end{bmatrix} \begin{bmatrix} x_1 \\ v_1 \\ x_2 \\ v_2 \\ x_3 \\ v_3 \end{bmatrix} + \begin{bmatrix} 0 \\ \frac{1}{m_{core}} \\ 0 \\ 0 \\ 0 \\ 0 \end{bmatrix} \frac{\tau}{r}$$

$$\begin{bmatrix} \frac{\theta}{r} \end{bmatrix} = \begin{bmatrix} x_0 \end{bmatrix} = \begin{bmatrix} 1 & 0 & 0 & 0 & 0 & 0 \end{bmatrix} \begin{bmatrix} x_1 \\ v_1 \\ x_2 \\ v_2 \\ x_3 \\ v_3 \end{bmatrix} + \begin{bmatrix} \frac{1}{k_{01}} \end{bmatrix} \frac{\tau}{r}$$

Where the equivalent spring constant between each point are as follows:

$$k_{01} = k_{34} = \frac{1}{\frac{1}{2k_{cable}} + \frac{1}{k_{core}}} \tag{3.4}$$

$$k_{12} = k_{RD} \tag{3.5}$$

$$k_{23} = \frac{1}{\frac{1}{k_{water}} + \frac{1}{k_{air}} + \frac{1}{k_{RD}}} \tag{3.6}$$

The resultant system is a 6th order state space model. The system can be represented with even higher-orders if the transmission components are broken down further. For example, the core is composed of five parts with different material properties, so the core could have been modelled as five separate springs. Doing so would increase the system order up to 14, which is impractical due to difficulty in experimental design to facilitate accurate model fitting up to such a high order.

Representing the system in lower orders is also possible, for example if the spring k_{23} was extremely stiff, the deflection of the third mass would be negligible. Therefore, the system can be further simplified to a 2-mass system, as shown in Figure 3.5. In this case, the state space system would be order 4.

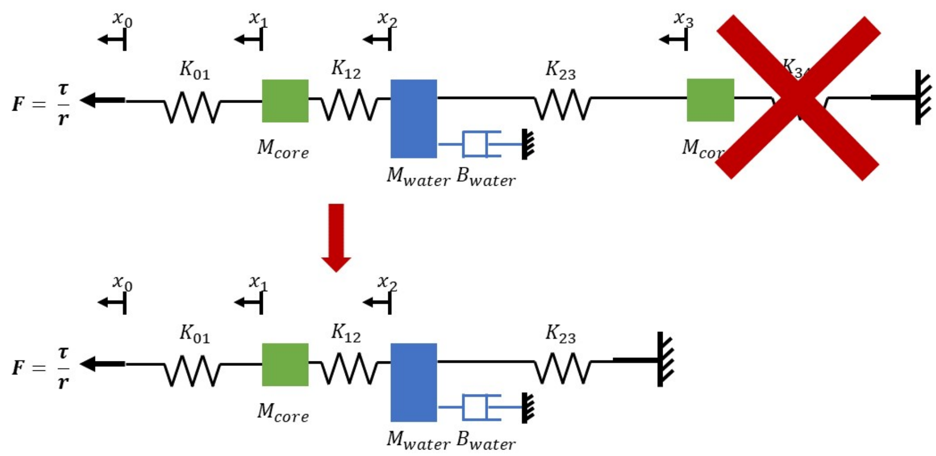

Figure 3.5: Transmission spring system model simplification in a case where the third mass has negligible oscillation. Spring constants are simplified according to equations 3.4, 3.5, and 3.6

The DC-gain of the system can represent the stiffness of the whole system, as shown in Equation 3.7

$$G(s=0) = \frac{\theta(s=0)}{\tau(s=0)} = \frac{1}{K_{bulk}} \tag{3.7}$$

This allows for performance comparisons against other rolling diaphragm transmissions [WW20], [GDL$^+$18], [GFC19], [BF20], [MW19], [WGBH14], which tend to report a bulk experimental whole-transmission stiffness value.

3.2.2 Hankel Singular Values

The impulse response of a system $G_0(q)$ is described by it's impulse response coefficients:

$$G_0(q) = \sum_{k=0}^{\infty} g_0(k) q^{-k} \tag{3.8}$$

where the impulse response coefficients relate to the state space matrices like so:

$$g(t) = \begin{cases} D & ,t = 0 \\ CA^{t-1}B & ,t \geq 1 \end{cases} \tag{3.9}$$

For an n-th order impulse response the finite impulse response coefficients $g(k)$ where $k = 0, 1, ...n-1$ and $N_1 + N_2 = n-1$, the corresponding Hankel matrix of impulse response coefficients will be:

$$H = \begin{bmatrix} g(1) & g(2) & \cdots & g(N_2) \\ g(2) & \ddots & \ddots & \vdots \\ \vdots & \ddots & \ddots & \vdots \\ g(N_1) & \cdots & \cdots & g(N_1+N_2-1) \end{bmatrix} \tag{3.10}$$

can be rewritten in terms of A, B, and C like so:

$$H = \begin{bmatrix} CB & CAB & \cdots & CA^{N_2-1}B \\ CAB & \ddots & \ddots & \vdots \\ \vdots & \ddots & \ddots & \vdots \\ CA^{N_1-1}B & \cdots & \cdots & CA^{N_1+N_2-1}B \end{bmatrix} \tag{3.11}$$

which can be rewritten in terms of the observability and controllability matrices:

$$H = H_1 H_2 = \begin{bmatrix} C \\ CA \\ \vdots \\ CA^{N_1-1} \end{bmatrix} \begin{bmatrix} B & AB & \cdots & A^{N_2-1}B \end{bmatrix} \tag{3.12}$$

By the Caley-Hamilton theorem, the rank of the controllability and observability matrices, which is also the rank of the Hankel matrix, indicates the rank of the state space system.

When investigating an unknown system's system order, the Hankel matrix's singular values can be used to indicate the system order. Assuming a noiseless set of data, where a Hankel matrix order is chosen such that $n_{hankel} = n_{system} + n_{extra} \geq n_{system}$, performing a singular value decomposition of H gives:

$$H = U \sum V^T = U \begin{bmatrix} \sum_{system} & 0 \\ 0 & \sum_{extra} \end{bmatrix} V^T \tag{3.13}$$

Where $\sum_{extra} = 0$ since the first n_{system} rows and columns have already described all of the system. With noisy data, singular values beyond the system order will no longer be 0, but should still be low in magnitude. Therefore, by fitting a high order impulse response onto experimental data, the significant Hankel matrix singular values indicate the underlying system order.

3.3 Acknowledgements

Chapter 3, in part, has been submitted for publication of the material as it may appear in ICRA 2023, Hoi Man Lam, W. Jared Walker, Lucas Jonasch, Dimitri Schreiber, and Michael C. Yip, IEEE 2023. The thesis author was the primary investigator and author of this paper.

4 Experiments and Results

4.1 Experimental Setup

To characterize the system, experiments were conducted to fit a second-order spring model, and to understand the hysteresis and friction of the system. On the input side, the input shaft is actuated either by hand or by a motor (Maxon EC393023). Torque inputs are measured through a torque sensor (Futek TRS600) in the hand-actuated case, and estimated via the motor current draw in the motor actuated case. On the output side, a second torque sensor at the output shaft measures the torque output. Encoders (US Digital E5-2000) are fitted to both shafts to measure the angular deflection both into and out of the transmission.

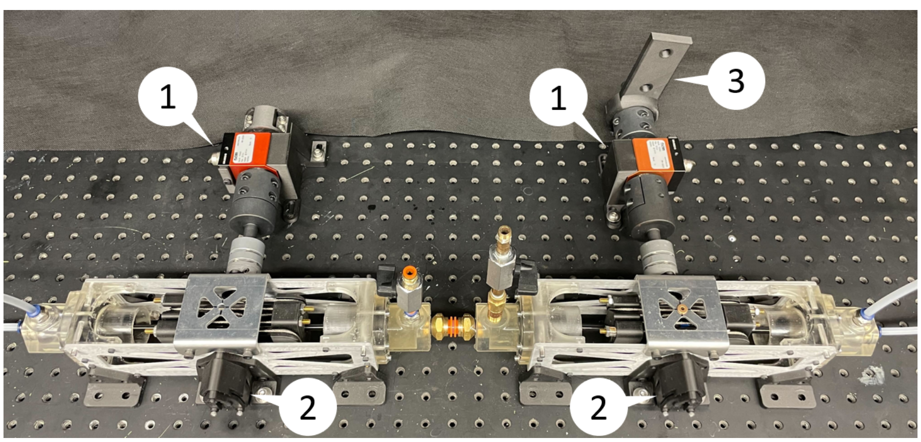

Figure 4.1: Experimental setup for hand-driven configuration. Shaft torques and positions are measured via torque sensors (1) and encoders (2). The input shaft is driven by a handle (3), or a motor can be substituted for motor-driven inputs.

The effects of hose length and diameter were minimized in this experiment by using a minimum hose length of $42.6mm$, to focus on the characteristics of the rolling diaphragm and cable drive. The system is bled of air bubbles until no more air can be visually seen in the system. The stiffness of shaft couples and torque sensors facilitating measurement are stiff enough to be disregarded in the stiffness estimation.

4.2 Experimental Model Order

The experimental system order of the transmission was investigated using a dataset where the output shaft clamped, while the input shaft is driven with a pseudo-random-phase-sequence (PRPS) torque signal. The motor-driven torque value and angular position of the input shaft are recorded and stored as *tfdata*, *impulseest* was used to estimate an impulse reposse, and the Hankel singular values of the impulse response coefficients were then computed and plotted.

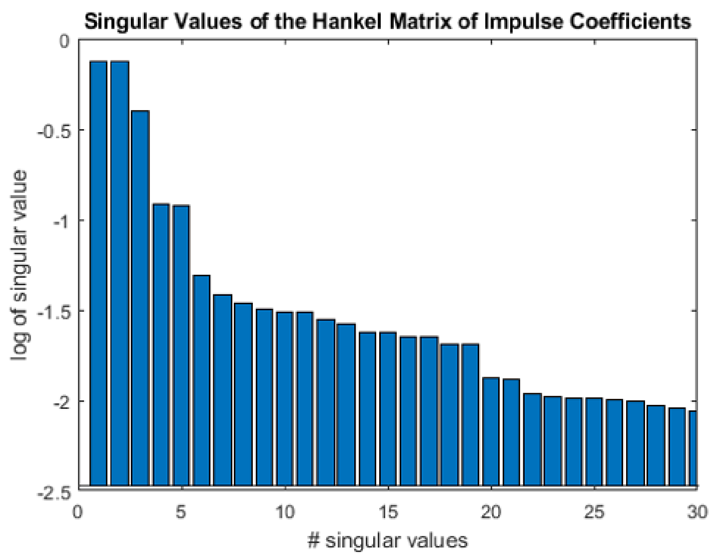

Figure 4.2: Hankel singular values of the impulse response coefficients between torque and angular position, from an experiment where a PRPS torque signal applied to the input shaft with a locked output shaft.

As explained previously, by examining the magnitude of the Hankel singular values, the model order of a system can be investigated by examining the minimum model order necessary for the magnitude of the singular value to approach zero. In Fig. 4.2, the first three or five impulse coefficients seems to capture the system well. From the compliance analysis, the low compliance contribution of the core and cables could mean that the output side core barely oscillates, which would explain why the 6th order onwards are not as significant.

However, though less significant, the magnitude of the singular values continues to decrease without tapering off asymptotically, indicating that use of additional states could still be useful. This could be due to how the system in reality is comprised of even more springs and masses, such as the core which was lumped as one mass and spring, but actually consists of multiple components made of different materials. This could also be due to a noisy dataset, where higher order modelling is instead starting to fit onto the noise rather than the actual transmission dynamics.

Another interesting observation is that the singular values show large drops in significance at 3 and 5 singular values, when one would expect that for typical coupled mass-spring-damper systems, the singular values should drop at even intervals. The reason for this is because in this system, the input is connected to the first mass via a spring. The system output position is also measured before that spring, which introduces the extra system order.

4.3 Frequency Domain Fitting

4.3.1 Raw Frequency Response

To collect frequency domain data, the output shaft is clamped, and the input shaft is driven with a pseudo-random-phase-signal (PRPS) was used to excite the system. Figure 4.3 shows the raw data collected from the experiment. The individual spikes are a result of the PRPS, which excites the system at uniformly spaced frequencies on a logarithmic scale, providing rich frequency domain excitation.

The resultant experimental frequency response is shown in Figure 4.4. The frequency response shows a resonance and anti-resonance, and although there seems to be

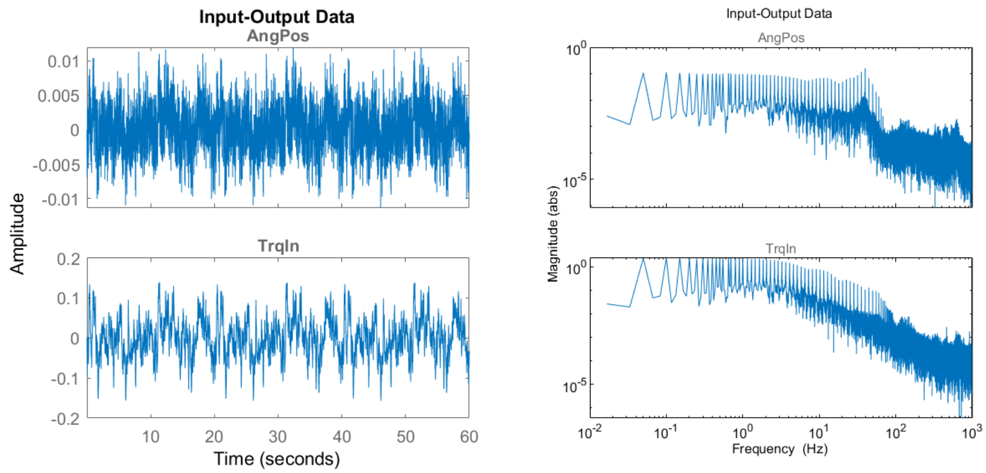

Figure 4.3: Raw angular position output and torque input data in the time and frequency domains. The input excitation is a PRPS.

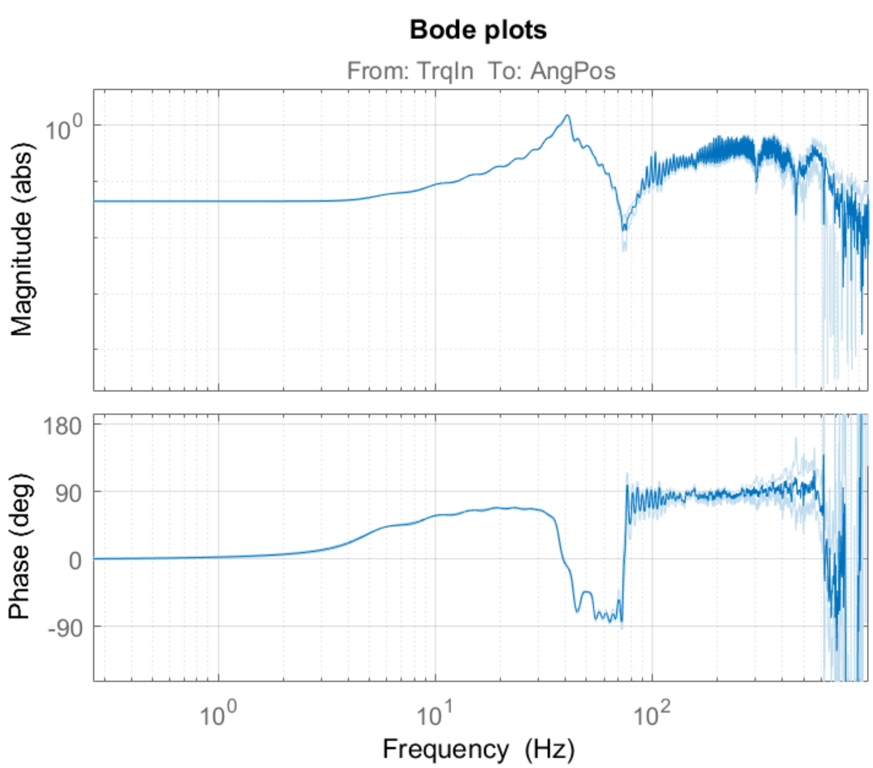

Figure 4.4: Bode plot of system response between angular position output and torque PRPS input.

some more resonant and anti-resonant behaviour towards the higher frequencies, the large amount of noise make it hard to tell. One interesting observation is that contrary to the typical coupled mass-spring-damper models, the frequency response exhibits an overall climb in magnitude and phase before the first resonance, rather than a flat response with resonances and anti-resonances.

An alternative model that could explain overall upwards trend in both magnitude and phase could be if the connection between the input force and the first mass was a spring and damper rather than just a spring, as illustrated in Figure 4.5.

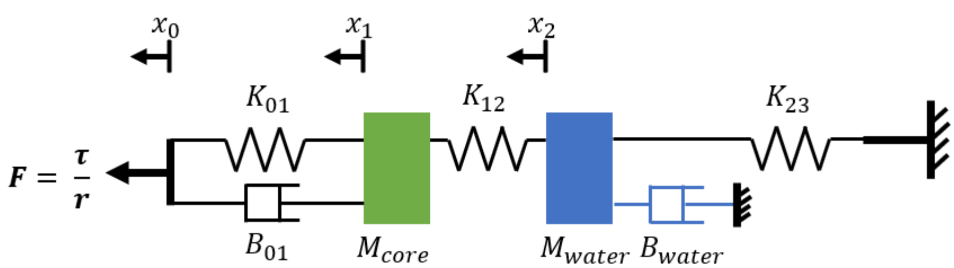

Figure 4.5: An alternate system where the input force is connected to the first mass via a spring and damper.

In this case, the transfer function will have a form with an order of 3 on the numerator, and an order 5 on the denominator, as shown in Equation 4.1. The existence of the $(K_{01} + B_{01}s)$ term on the numerator allows the response to exhibit the upwards slope shape that is seen on the experimental frequency response.

$$G(s) = \frac{1 + (M_{water}s^2 + B_{water}s + K_{01} + K_{12})(K_{01} + B_{01}s)}{(M_{water}s^2 + B_{water}s + K_{01} + K_{12})(M_{core}s^2 + K_{23})(K_{01} + B_{01}s)} \tag{4.1}$$

4.3.2 Frequency Domain Model Fit

A *ssest* was performed with measured torque and position as input and output, starting from an initial model based on parameters from prior theoretical calculations (Table 4.1). An emphasis is placed on the lower frequency range by applying a weighting window between the 0 to 180 Hz range, as the high-magnitude noisy behaviour at the upper frequencies is less important. The 6th and 5th order models both fit essentially the same way in the lower frequency range, successfully capturing the frequency response.

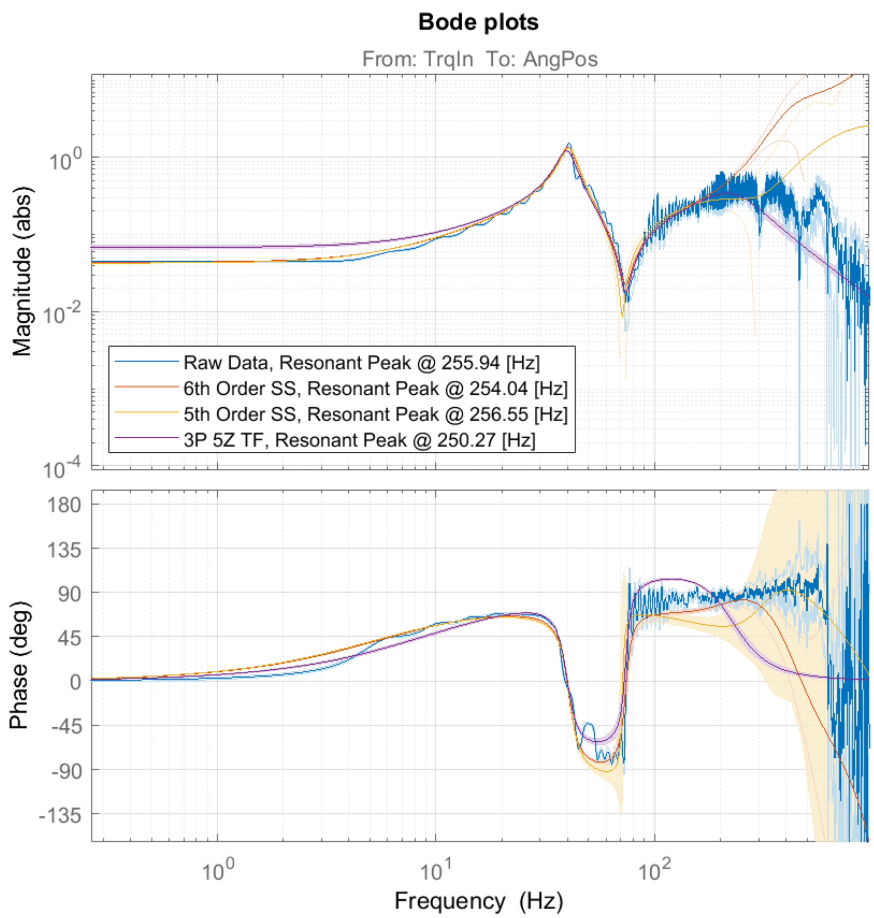

Figure 4.6: Frequency response fit with state space models of order 6 and 5, and a transfer function model with 3 poles and 5 zeros.

A *tfest* was also applied based on the system described in Figure 4.5 and Equation 4.1. This model also captures the primary resonance and anti-resonance, but does better than the state space fits in the noisy high-frequency regime by matching the overall downward slope in magnitude. However, the dc-gain does not match as well compared to the state space models.

Table 4.1: Fit results of state-space and transfer function models on PRPS frequency data

Model	Bulk Stiffness	Resonant Frequency	Antiresonant Frequency	Fit Quality
6th Order SS	22.95 $[Nm/rad]$	254.0 $[Hz]$	2660.9 $[Hz]$	93.62%
5th Order SS	23.45 $[Nm/rad]$	256.5 $[Hz]$	2949.1 $[Hz]$	92.83%
3P 5Z TF	14.68 $[Nm/rad]$	250.2 $[Hz]$	1439.5 $[Hz]$	76.39%

The resultant fits (Table 4.1) show similar resonant frequencies, but differing antiresonant frequencies. This might be due to difficulties in pinpointing the antiresonant node with the larger amount of noise at the higher frequencies.

The bulk stiffnesses for both state space models are around $23[Nm/rad]$, which are extremely close to the theoretical bulk stiffness of $23.54[Nm/rad]$. However, the transfer function model did not successfully capture the dc-gain, resulting in a lower bulk stiffness estimate.

Additionally, hand-actuated datasets were collected for model validation, measuring input torque applied and input shaft deflection. The model predicted position tracks the measured position somewhat in Fig. 4.7, performing better in the lower frequency motion regions. However, between 25 to 42.5 seconds, the high-frequency jittery torque input causes problems for the models, which do not have good frequency response fits at high frequencies.

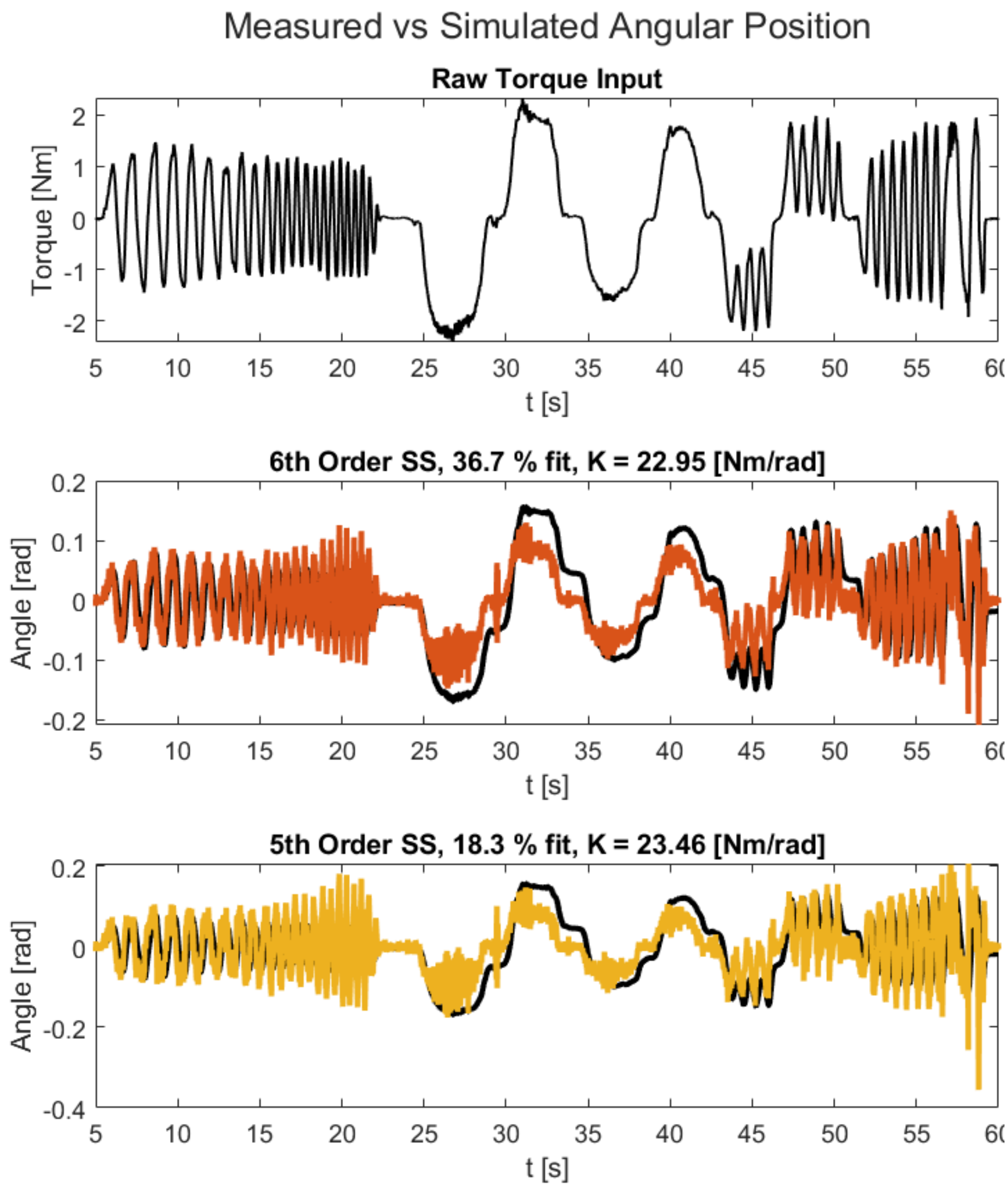

Figure 4.7: Verification of fitted model against the hand-driven dataset, where the simulated position from measured input torque is compared against the measured position.

4.4 Hysteresis

From a hysteresis plot of one torque sin wave motion from rest (Fig. 4.8), there is an approximate maximum hysteresis value of $0.076Nm$, corresponding to 1.25% of the full $6Nm$ torque range. This hysteresis is likely caused by hose flexibility or air line pressure regulation inaccuracy, which affects shaft phasing, absorbs input energy, and has directional behaviour under positive and negative pressures. Another possibility is inaccurate pressure regulation or air leakage in the air line, leading to volume and pressure variance during the motion. The static friction, identified by the change in torque without change in angular position at either end of the hysteresis curve, is $0.025Nm$, corresponding to 0.45% of the full torque range. Though the rolling diaphragm has little static friction, some other elements such as the cable drive and bearings still contribute to static friction.

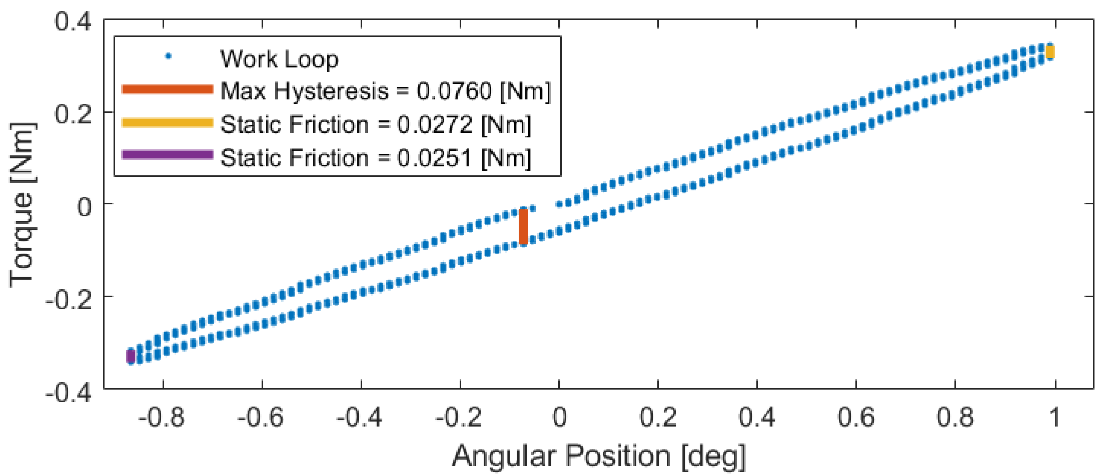

Figure 4.8: Hysteresis plot of one torque sin wave input starting from rest, maximum hysteresis measured is $0.0760Nm$ (1.27% of $6Nm$ full torque range), and maximum static friction measured is $0.0272Nm$ (0.45% of $6Nm$ full torque range).

4.5 Position and Torque Tracking

To compare the tracking accuracy between the input and output shafts, the transmission was actuated across a large range of motion by hand via a handle on the input shaft, while a load with inertia $0.0387kgm^2$ is attached to the output shaft (Fig. 4.9). The results show good tracking over the entire motion, with slight tracking error at the position and torque extremities that are likely caused by hysteresis and energy losses. The close tracking between the input and output torques validate the transmission's constant mechanical advantage across a large range of motion. Close position and torque tracking is especially important in use cases such as intraoperative CT/MRI surgical robotics, where it might not be possible to recieve sensor feedback of joint position and torque from within the CT/MRI bore.

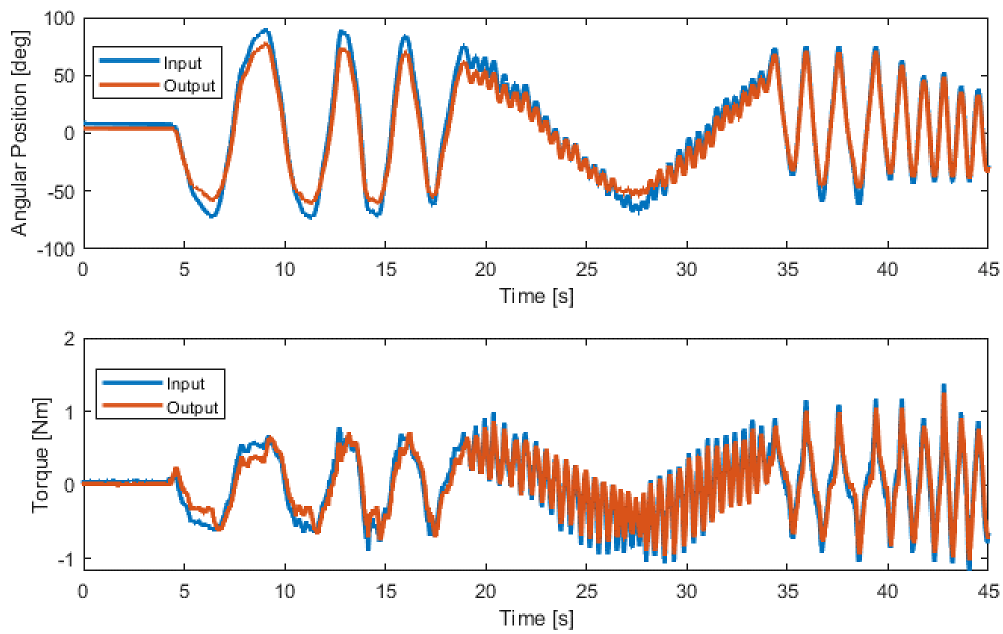

Figure 4.9: Transmission input/output shaft angular position and torque over time, where input shaft is actuated by hand and output shaft is loaded with an inertia of $0.0387kgm^2$.

4.6 Acknowledgements

Chapter 4, in part, has been submitted for publication of the material as it may appear in ICRA 2023, Hoi Man Lam, W. Jared Walker, Lucas Jonasch, Dimitri Schreiber, and Michael C. Yip, IEEE 2023. The thesis author was the primary investigator and author of this paper.

5 Conclusion

In this thesis, a rolling diaphragm transmission featuring a coaxial opposed rolling diaphragm layout, and a translating core enclosed cable drive, was prototyped and tested. The prototype displays low hysteresis, low friction, and good position and torque transparency. An automated transmission pressurization and phasing system was also detailed, improving the ease of system setup and maintenance.

According to the theoretical stiffness model, minuscule amounts of undissolved air can have a significant impact on system stiffness. Apart from undissolved air, the rolling diaphragm stiffness contributes the most to system compliance, forming a 'bottom line' on transmission stiffness.

Further investigation into methods to thoroughly dissolve and bleed air in the transmission, as well as stiffer diaphragm choice, can greatly improve system stiffness. Further understanding the rolling diaphragm in isolation, such as it's damping and rolling friction, may also help identify other design limitations for rolling diaphragm based transmissions.

Bibliography

[BF20] Marco Bolignari and Marco Fontana. Design and experimental characterization of a high performance hydrostatic transmission for robot actuation. *Meccanica*, 55(5):1169–1179, May 2020.

[BI10] Ozgur Baser and E. Ilhan Konukseven. Theoretical and experimental determination of capstan drive slip error. *Mechanism and Machine Theory*, 45(6):815–827, 2010.

[DGL+17] Z. Dong, Ziyan Guo, Kit-Hang Lee, M. C. Leong, Chim-Lee Cheung, A. Lee, W. Luk, and K. Kwok. A Robotic Catheter System for MRI-guided Cardiac Electrophysiological Intervention. https://www.semanticscholar.org/paper/A-Robotic-Catheter-System-for-MRI-guided-Cardiac-Dong-Guo/96fd3cdd07dab175c01c82f902b7066ef870976a, 2017.

[DGL+19] Ziyang Dong, Ziyan Guo, Kit-Hang Lee, Ge Fang, Wai Lun Tang, Hing-Chiu Chang, Danny Tat Ming Chan, and Ka-Wai Kwok. High-Performance Continuous Hydraulic Motor for MR Safe Robotic Teleoperation. *IEEE Robotics and Automation Letters*, 4(2):1964–1971, April 2019.

[DPG21] Jeff Denis, Jean-Sébastien Plante, and Alexandre Girard. Low-Level Force-Control of MR-Hydrostatic Actuators. *IEEE Robotics and Automation Letters*, 6(2):3849–3856, April 2021.

[FIS+21] Samuel Frishman, Robert D. Ings, Vipul Sheth, Bruce L. Daniel, and Mark R. Cutkosky. Extending Reach Inside the MRI Bore: A 7-DOF, Low-Friction, Hydrostatic Teleoperator. *IEEE Transactions on Medical Robotics and Bionics*, 3(3):701–713, August 2021.

[GDL+18] Ziyan Guo, Ziyang Dong, Kit-Hang Lee, Chim Lee Cheung, Hing-Choi Fu, Justin D.L. Ho, Haokun He, Wai-Sang Poon, Danny Tat-Ming Chan, and Ka-Wai Kwok. Compact Design of a Hydraulic Driving Robot for Intraoperative MRI-Guided Bilateral Stereotactic Neurosurgery. *IEEE Robotics and Automation Letters*, 3(3):2515–2522, July 2018.

[GFC19] Alexander Gruebele, Samuel Frishman, and Mark R. Cutkosky. Long-Stroke Rolling Diaphragm Actuators For Haptic Display of Forces in Teleoperation. *IEEE Robotics and Automation Letters*, 4(2):1478–1484, April 2019.

[HR96] R.E. Hobbs and M. Raoof. Behaviour of cables under dynamic or repeated loading. *Journal of Constructional Steel Research*, 39(1):31–50, 1996. Special Issue on Tension Structures.

[KCGP20] Charles Khazoom, Pierre Caillouette, Alexandre Girard, and Jean-Sébastien Plante. A supernumerary robotic leg powered by magnetorheological actuators to assist human locomotion. *IEEE Robotics and Automation Letters*, 5(4):5143–5150, 2020.

[mar] Rolling diaphragm operation. *www.belloframdiaphragm.com/ diaphragm-operation.*

[MW19] Evelyn Mendoza and John Peter Whitney. A Testbed for Haptic and Magnetic Resonance Imaging-Guided Percutaneous Needle Biopsy. *IEEE Robotics and Automation Letters*, 4(4):3177–3183, October 2019.

[VDL+20] Catherine Véronneau, Jeff Denis, Louis-Philippe Lebel, Marc Denninger, Vincent Blanchard, Alexandre Girard, and Jean-Sébastien Plante. Multifunctional Remotely Actuated 3-DOF Supernumerary Robotic Arm Based on Magnetorheological Clutches and Hydrostatic Transmission Lines. *IEEE Robotics and Automation Letters*, 5(2):2546–2553, April 2020.

[WCMH16] John P. Whitney, Tianyao Chen, John Mars, and Jessica K. Hodgins. A hybrid hydrostatic transmission and human-safe haptic telepresence robot. In *2016 IEEE International Conference on Robotics and Automation (ICRA)*, pages 690–695, May 2016.

[WGBH14] John P. Whitney, Matthew F. Glisson, Eric L. Brockmeyer, and Jessica K. Hodgins. A low-friction passive fluid transmission and fluid-tendon soft actuator. In *2014 IEEE/RSJ International Conference on Intelligent Robots and Systems*, pages 2801–2808, September 2014.

[WW20] Chunpeng Wang and John P. Whitney. Series Elastic Force Control for Soft Robotic Fluid Actuators. *arXiv:2004.01269 [cs]*, April 2020.